PLOS | COMPUTATIONAL BIOLOGY

RESEARCH ARTICLE

# Hydrophobic Gating of Ion Permeation in Magnesium Channel CorA

**Chris Neale[1,2], Nilmadhab Chakrabarti[1], Pawel Pomorski[3], Emil F. Pai[2,4,5,6], Régis Pomès[1,2]***

**1** Molecular Structure and Function, The Hospital for Sick Children, Toronto, Ontario, Canada, **2** Department of Biochemistry, University of Toronto, Toronto, Ontario, Canada, **3** Shared Hierarchical Academic Research Computing Network, Department of Physics and Astronomy, University of Waterloo, Waterloo, Ontario, Canada, **4** Department of Medical Biophysics, University of Toronto, Toronto, Ontario, Canada, **5** Department of Molecular Genetics, University of Toronto, Toronto, Ontario, Canada, **6** Ontario Cancer Institute/Princess Margaret Cancer Centre, Campbell Family Institute for Cancer Research, Toronto, Ontario, Canada

* pomes@sickkids.ca



OPEN ACCESS

**Citation:** Neale C, Chakrabarti N, Pomorski P, Pai EF, Pomès R (2015) Hydrophobic Gating of Ion Permeation in Magnesium Channel CorA. PLoS Comput Biol 11(7): e1004303. doi:10.1371/journal.pcbi.1004303

**Editor:** Emad Tajkhorshid, University of Illinois, UNITED STATES

**Received:** September 16, 2014

**Accepted:** April 28, 2015

**Published:** July 16, 2015



**Data Availability Statement:** All relevant data are within the paper and its Supporting Information files.

**Funding:** CN is funded by a postdoctoral fellowship from the Canadian Institutes of Health Research, by the Research Training Center at the Hospital for Sick Children, and by the University of Toronto. PP is funded by SHARCNET. EFP holds a Canada Research Chair. This work was funded in parts by Canadian Institutes of Health Research Operating Grants MOP-86548, MOP-43949, and MOP-43998, and by the Ontario Ministry of Health and Long Term Care. The views expressed do not necessarily reflect those of OMOHLTC. SciNet is funded by the Canada

## Abstract

Ion channels catalyze ionic permeation across membranes via water-filled pores. To understand how changes in intracellular magnesium concentration regulate the influx of $Mg^{2+}$ into cells, we examine early events in the relaxation of $Mg^{2+}$ channel CorA toward its open state using massively-repeated molecular dynamics simulations conducted either with or without regulatory ions. The pore of CorA contains a 2-nm-long hydrophobic bottleneck which remained dehydrated in most simulations. However, rapid hydration or "wetting" events concurrent with small-amplitude fluctuations in pore diameter occurred spontaneously and reversibly. In the absence of regulatory ions, wetting transitions are more likely and include a wet state that is significantly more stable and more hydrated. The free energy profile for $Mg^{2+}$ permeation presents a barrier whose magnitude is anticorrelated to pore diameter and the extent of hydrophobic hydration. These findings support an allosteric mechanism whereby wetting of a hydrophobic gate couples changes in intracellular magnesium concentration to the onset of ionic conduction.

## Author Summary

This study shows how rapid wetting/dewetting transitions in the pores of ion channels participate in the control of biological ion permeation. Ion channels catalyze ionic permeation across non-polar membranes via water-filled pores. However, non-polar stretches or hydrophobic bottlenecks are present in the pores of many ion channels. To clarify the relationship between channel regulation, pore hydration, and ion permeation, we examine how the slow relaxation of magnesium channel CorA from its closed state towards its open state modulates wetting of its hydrophobic bottleneck. Results provide a quantitative description of wetting and dewetting probabilities and kinetics and a quantitative relationship between the extent of pore hydration and the energetics of ion permeation, consistent with a mechanism of hydrophobic gating.

Foundation for Innovation (CFI) under the auspices of Compute Canada; the Government of Ontario; Ontario Research Fund - Research Excellence; and the University of Toronto. The funders had no role in study design, data collection and analysis, decision to publish, or preparation of the manuscript.

**Competing Interests:** The authors have declared that no competing interests exist.

## Introduction

Magnesium homeostasis is essential for life. In humans, the misregulation of magnesium is implicated in stroke [1], heart disease [2], and diabetes [3]. Magnesium transport is also crucial for bacteria [4]. The movement of magnesium through cell membranes, like that of other ions, is accomplished by integral membrane proteins that provide selective permeability across the dielectric barrier of the lipid bilayer [5]. In bacteria, magnesium uptake is mediated by the CorA protein [6–9], which can substitute for its functional homologue in yeast mitochondria [10]. Electrophysiological data suggests that TmCorA is a channel, not a transporter [8].

Seven crystallographic structures exist for CorA, six of which are from *Thermotoga maritima* (TmCorA) [11–16]. These structures reveal a homopentamer in which 10-nm-long protomeric α-helices (the "stalk" helices) form a transmembrane (TM) pore through which magnesium is presumed to flow. This pore contains two hydrophobic constrictions: the "MM stretch" (MM), a 1.9-nm-long constriction formed by pore-lining residues M291, L294, A298, and M302; and the "lower leucine constriction" (LC), a shorter steric bottleneck formed by the sidechain of L280 (Fig 1). Mutagenesis studies suggest that the MM, but not the LC, is involved in channel gating [17, 18]. Hydrophobic gates are important for the function of many ion channels, including ligand-gated [19–22], voltage-gated [23, 24], phosphorylation-gated [25], and mechanosensitive channels [26, 27].

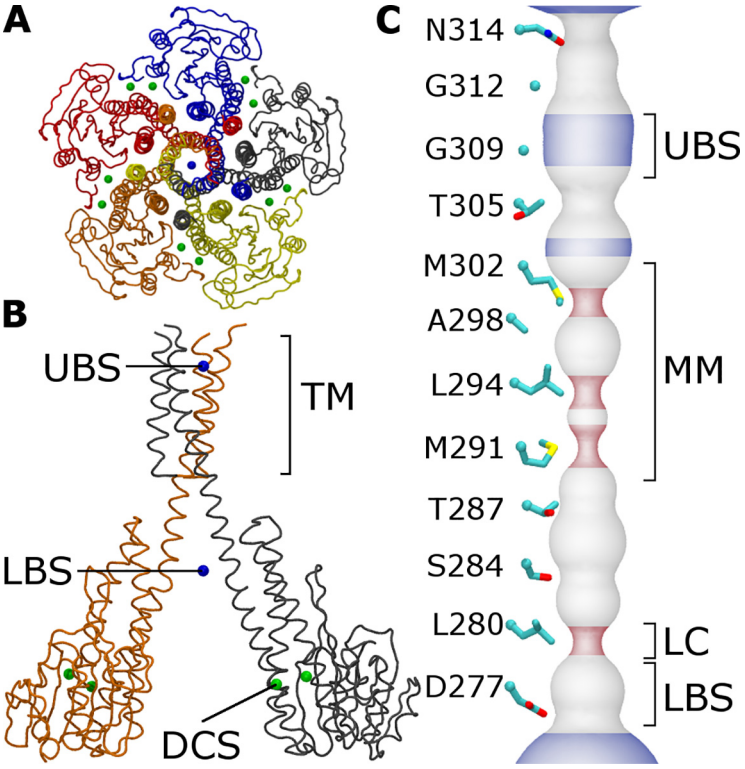


**Fig 1. Structural features of the TmCorA protein.** (A) Backbone trace of TmCorA viewed along the pore axis from the extracellular side, colored by protomer. Divalent cations in the 2HN2 crystal structure [13] are shown as spheres for (green) regulatory cations and (blue) cations inside the pore. (B) Side view of two protomers. Annotations include cation binding sites in the cytoplasmic domain and the upper and lower regions of the pore (respectively DCS, UBS, and LBS) and the transmembrane region (TM). (C) Surface representation of the pore diameter in the 2HN2 crystal structure [13]. The lower leucine constriction (LC) is indicated. The pore is colored by its local diameter, which is either (blue) larger than that of hexahydrated magnesium (0.68 nm), (red) smaller than that of a single water molecule (0.28 nm), or (grey) intermediate.

doi:10.1371/journal.pcbi.1004303.g001

In all crystal structures of CorA, both hydrophobic constrictions are too narrow to be hydrated, suggesting that the channel is in its closed state. Remarkably, the pore extends beyond the relatively small TM domain into a much larger funnel-shaped domain that protrudes by 6 nm into the cytosol (Fig 1). At the far rim of this funnel, divalent cations are bound between cytosolic protomer interfaces (the divalent cation sensor or DCS; Fig 1). Based on crystallographic structures, it was hypothesized that divalent cation occupancy of the DCS regulates magnesium transport by controlling the pore's diameter or electrostatic profile [11–13]. Recent studies suggest that divalent cation binding to the DCS locks TmCorA in a transport incompetent conformation and that loss of these cations leads to an open conformation of the channel [14, 28], which may be asymmetric [14].

To investigate the allosteric regulation of pore opening, we previously conducted a molecular dynamics (MD) study of TmCorA in a hydrated lipid bilayer, either with or without $Mg^{2+}$ ions in the DCS [29]. The MM remained dehydrated throughout a 110-ns MD simulation in the presence of regulatory ions, but became dilated and hydrated in one of two trajectories generated after these ions were removed [29]. Wetting of the MM involved an iris-like mechanism initiated by the rearrangement of the cytosolic domain interfaces and transmitted to the MM by the long pore-lining stalk helices. These findings suggest a model of allosterically-regulated hydrophobic gating whereby decreasing cytosolic magnesium concentration reduces magnesium occupancy in the DCS, leading to sudden wetting of the pore.

Here, we use massive sampling to examine the statistical significance and the kinetics of this apparent hydrophobic gating process, and to assess whether it results in the open state of the channel. Scaling up computational sampling by two orders of magnitude, we compare hundreds of 35-ns MD simulations in which the DCS are either fully occupied or empty. From a total of 54 microseconds of sampling, we observe many events in which completely connected columns of water condense and evaporate in the MM. We show that this hydrophobic gate is more likely to become hydrated in the absence of regulatory ions and we quantify the kinetics of wetting and dewetting transitions. Finally, we show that the extent of hydration of the MM is correlated to a reduction in the free energy barrier for the permeation of $Mg^{2+}$ ions, supporting the hypothesis that the MM is an allosterically-regulated hydrophobic gate.

## Results

### Hydrophobic Hydration

To determine the kinetics of allosterically-regulated wetting in the MM (the presumed hydrophobic gate), we massively repeated MD simulations of TmCorA in the two limiting states of ionic regulation, namely, with all ten regulatory (DCS) binding sites either occupied or empty. The PDB:2HN2 crystallographic structure of TmCorA [13] was embedded in a hydrated lipid bilayer and seven-hundred 35-ns MD simulations were conducted for each regulatory state. Initially, water filled most of the pore but the MM and the LC were completely dehydrated. Although the MM remained dehydrated in most of the simulations, it was hydrated at least part of the time in 12 and 25% (respectively 83 and 175) of the 700 simulations conducted respectively with and without regulatory ions (Table 1), allowing us to quantify the effect of regulatory ions on pore hydration. MM wetting is depicted as S1 Movie. In wetting transitions, water molecules entered the MM along the pore axis and, occasionally, through transient packing defects between pore-lining helices. The latter defects connected the middle of the pore directly to bulk water at the cytosolic membrane-water interface (S1 Fig).

To characterize wetting, we computed the maximum distance between consecutive water oxygen atoms along the pore axis, $z_{gap}$. Wetting in the MM or LC is defined as end-to-end hydration by a completely connected water column ($z_{gap} \leq 0.38$ nm). The fraction of

**Table 1. Number of simulations in which the MM was wetted for increasingly large percentages of the trajectory.**

| % of trajectory hydrated (ns in brackets) | *N* simulations meeting criterion | | |
|---|---|---|---|
| | Regulatory ions | | ratio[a] |
| | no | yes | |
| >0 (0) | 175 | 83 | 2.1 |
| ≥0.05 (0.18) | 100 | 31 | 3.2 |
| ≥1 (0.35) | 78 | 25 | 3.1 |
| ≥5 (1.75) | 28 | 6 | 4.7 |
| ≥10 (3.5) | 13 | 4 | 3.2 |
| ≥20 (7) | 10 | 1 | 10 |

[a]*N*(no reg. ions) / *N*(reg. ions)

doi:10.1371/journal.pcbi.1004303.t001

simulations in which the MM was wetted, $P(z_{gap} \leq 0.38\ nm)$, is shown as a function of simulation time in Fig 2A. In the presence of regulatory ions, this fraction appears to stabilize around 0.3% after 15 ns (Fig 2A). In contrast, the MM was wetted five times more often in the absence of regulatory ions, and the wetting probability increased from 0 to 2% through the entire length

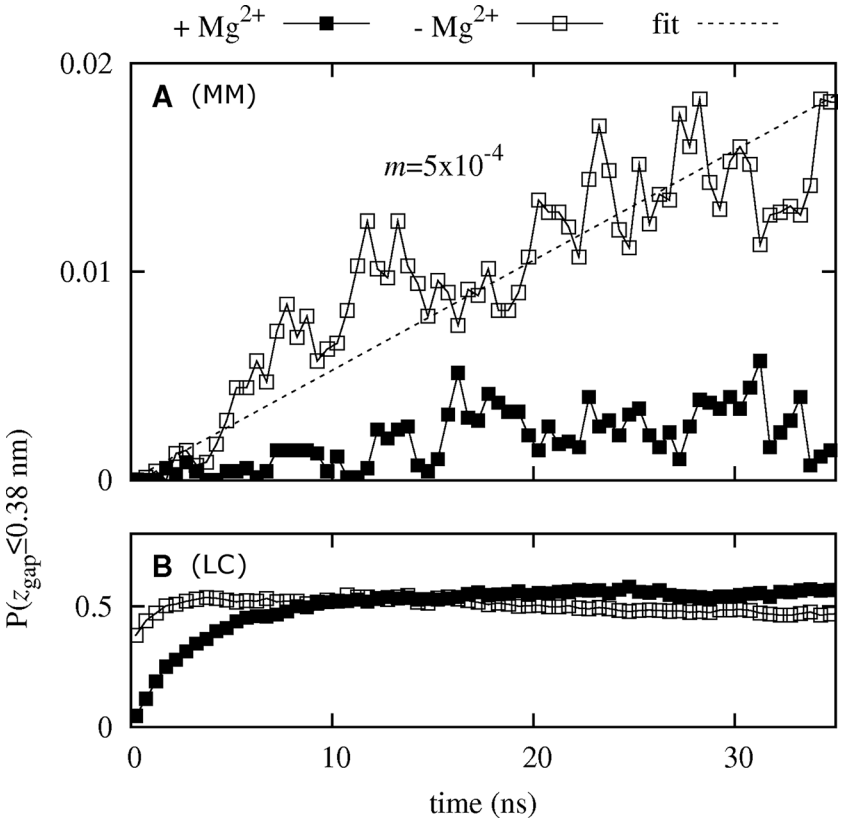


**Fig 2. Pore hydration.** Fraction of simulations with a completely connected water column, $P(z_{gap} \leq 0.38\ nm)$, in (A) the MM and (B) the LC as a function of simulation time. Results based on all simulations are shown for systems (filled squares) with regulatory ions and (empty squares) without regulatory ions. A linear fit is indicated by a broken line.

doi:10.1371/journal.pcbi.1004303.g002

of the simulations (Fig 2A). Conversely, hydration of the LC increased from 0 to 50% independently of ionic occupancy of the DCS, although equilibration occurred more rapidly in the absence of regulatory ions (Fig 2B).

## Extent of Pore Hydration

To quantify the extent of hydration of the hydrophobic constrictions, we used two metrics, the length of the longest dehydrated stretch, $z_{gap}$, and the number of water molecules, $N_{wat}$. As expected, these two metrics are strongly anti-correlated (S2A and S2E Fig). The normalized distributions of $z_{gap}$ (S2B and S2F Fig) and $N_{wat}$ (S2C and S2G Fig) in the MM were similar for the two sets of simulations. Hydration defects were most common near M291, at the cytosolic end of the MM (S2D and S2H Fig). These findings are consistent with our previous simulations [29] and with the hypothesis of Lunin *et al.* that M291 and L294 form the main hydrophobic gate [11]. Finally, S3 Fig shows that hydration of the MM and LC pore constrictions are not correlated with each other.

In both regulatory states, many of the wetting events were transient, half of them lasting less than 200 ps. For each simulation, Fig 3 shows the fraction of time that the MM was wetted as a function of the fraction of time that the MM contained >20 water molecules. This analysis leads us to identify eight simulations in which the MM was both stably and highly hydrated, all of which occurred in the absence of regulatory ions. These simulations are henceforth referred to as "stably superhydrated" (SSH).

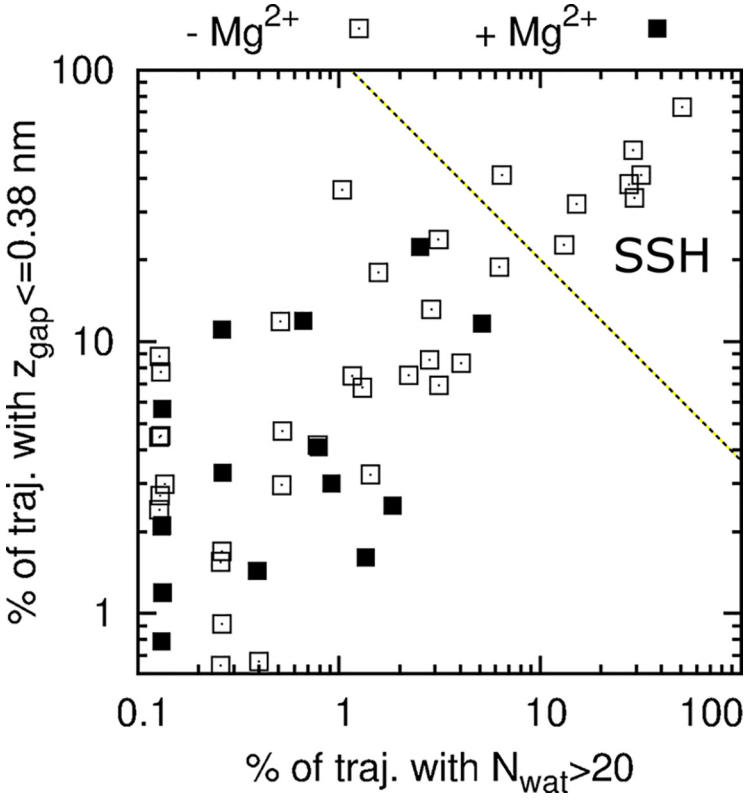


**Fig 3. Stability vs. extent of hydration.** The percentage of each simulation in which $N_{wat}$>20 is plotted against the percentage of that simulation in which $z_{gap} \leq 0.38$ nm. Each point represents a simulation in which regulatory ions are present (filled squares) or absent (open squares). Note that many of the 1,400 simulations are not visible because their MM remained dry. The dividing line between transiently and stably superhydrated (SSH) simulations was selected by eye.

doi:10.1371/journal.pcbi.1004303.g003

In the most hydrated SSH simulation, the initially dehydrated MM abruptly and durably filled with ≥20 water molecules, at one point surging to twice this amount (Fig 4A). This hydration was concurrent with an increase in mean MM pore diameter from 0.4 to 0.74 nm (Fig 4A–4C) and involved asymmetric reorientation of pore-lining sidechains away from the lumen, toward neighboring protomers (Fig 4D and 4E).

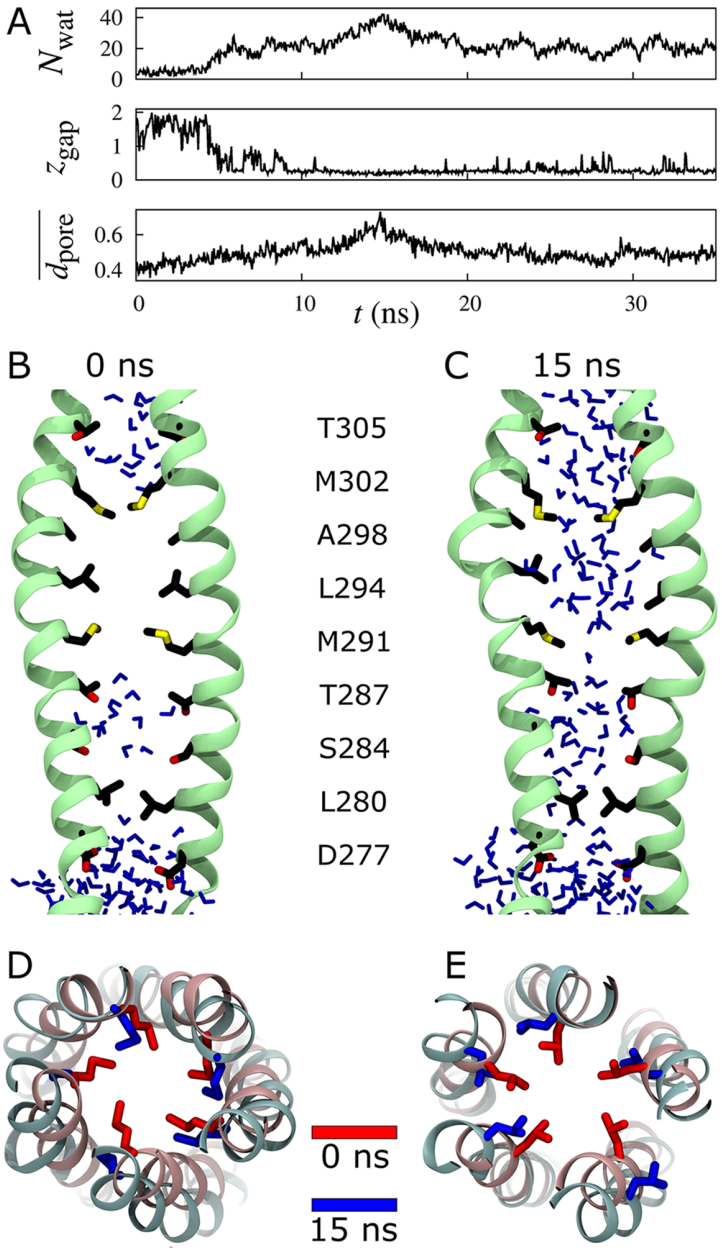


**Fig 4. Wetting and pore dilation in the most hydrated SSH simulation.** (A) Number of water molecules, $N_{wat}$, length of the largest dehydration, $z_{gap}$, and average pore diameter, $\overline{d_{pore}}$, in the MM as functions of simulation time $t$ ($z_{gap}$ and $\overline{d_{pore}}$ are in nm). Similar plots for all eight SSH simulations and representative simulations with and without regulatory ions are shown in S4 and S5 and S6 Figs, respectively. (B, C) Side view of two TmCorA protomers highlighting pore-lining sidechains and lumenal water molecules at (B) 0 and (C) 15 ns. (D, E) Extracellular view along the pore axis showing sidechains of (D) M302 and (E) L294 at (red) 0 and (blue) 15 ns.

doi:10.1371/journal.pcbi.1004303.g004

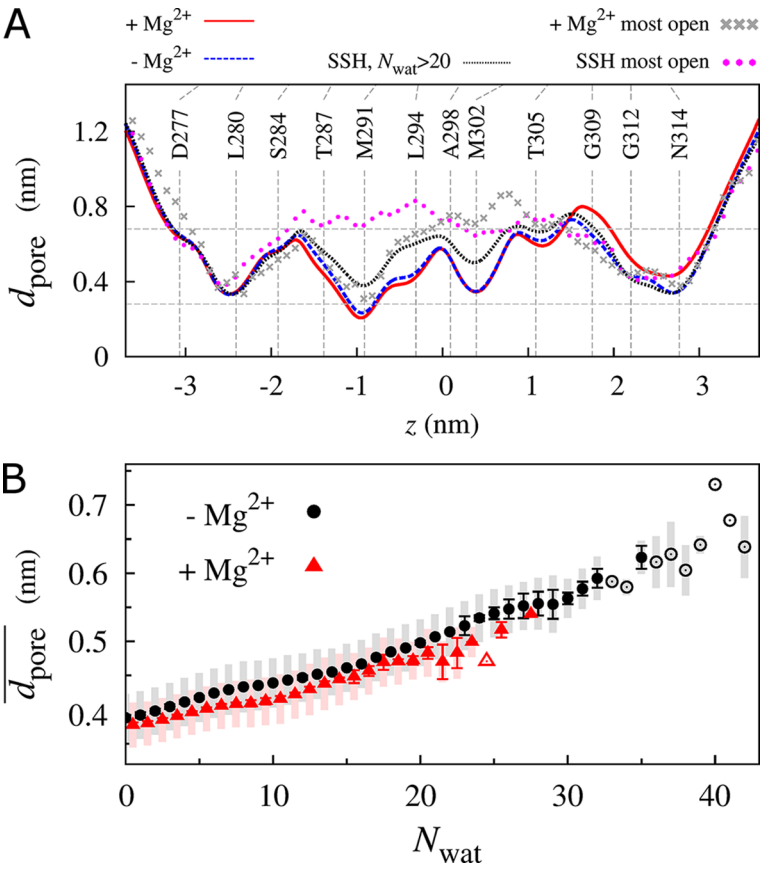


**Fig 5. Swelling and hydration of the pore.** (A) Pore diameter, $d_{pore}$, along the pore axis, $z$. Average values from all simulations (solid red line) with and (broken blue line) without regulatory ions; (dotted black line) conformations with $N_{wat}$>20 in all eight SSH simulations; and single conformation with the largest values of mean pore diameter in the MM, $\overline{d_{pore}}$, from simulations (grey x symbols) with and (magenta circles) without regulatory ions. Vertical lines indicate average positions of terminal heavy atoms of pore-lining sidechains, connecting above residue labels to lines that extend to average $C_\alpha$ atom positions. Horizontal lines indicate the diameters of hexahydrated $Mg^{2+}$ and water. The value $z = 0$ corresponds to the center of mass of MM backbone atoms. (B) $\overline{d_{pore}}$ as a function of $N_{wat}$ for simulations (red triangles) with and (black circles) without regulatory ions. Shaded regions enclose one standard deviation of sampled values and error bars represent the uncertainty as the standard deviation of the mean after dividing the trajectories into two sets. Empty symbols denote an inability to assess the uncertainty because the corresponding value of $N_{wat}$ was only sampled in one simulation block. Data for simulations with regulatory ions are offset by +0.5 $N_{wat}$ units for clarity.

doi:10.1371/journal.pcbi.1004303.g005

To assess whether hydration was coupled to reorganization of the pore, we computed the pore diameter along its long axis. On average, the volume available in the MM did not substantially depend on regulatory ion occupancy in the DCS (Fig 5A). However, SSH simulations displayed an increase in MM diameter concurrent with wetting. The mean pore diameter in the MM occasionally fluctuated above 0.68 nm (the diameter of a hexahydrated $Mg^{2+}$ ion) in the absence of regulatory ions, but never in their presence (Fig 5A). Upon removal of these ions, there was, on average, a tightening of the pore at its extracellular end, near the proposed selectivity filter of the GMN motif [30] (Fig 5A). Regardless of regulatory ion occupancy, the mean pore diameter in the MM was linearly correlated to the extent of hydration (Fig 5B).

It has been suggested that MM wetting could be triggered by the exposure of previously-hidden hydrophilic moieties to the pore lumen following axial rotation of the stalk helices [15, 16].

To test this hypothesis, we analyzed protein-water hydrogen bond interactions in the MM (S1 Text and S7 and S8 Figs). Taken together, our analysis indicates that pore wetting is not due to a decrease in the hydrophobic character of the MM but rather that its likelihood increases with the volume of the hydrophobic stretch. Accordingly, the increase in both wetting probability and hydration number with CorA pore size is consistent with hydrophobic wetting in simple nanoscopic systems [31] and in hydrophobic pore analogs such as carbon nanotubes [32]. The sharp dependence of hydrophobic wetting on dynamic fluctuations in pore diameter makes this process well suited to gating in a biological channel.

Distributions of $N_{wat}$ are shown in Fig 6A. Despite the presence of wetting transitions, these distributions are unimodal and values of $N_{wat}$ greater than 10 are rare. The most likely value of $N_{wat}$ in the MM is 2 for simulations both with and without regulatory ions (Fig 6A). The distribution of $N_{wat}$ is shifted to slightly larger values in the absence of regulatory ions, a shift that persists after the removal of the SSH simulations from this analysis (Fig 6A). The distribution of $N_{wat}$ computed exclusively from the SSH simulations is bimodal, with maxima at $N_{wat}$ = 3 and 20 (Fig 6A). Fig 6B shows the distribution of hydration number computed separately for the wetted state. In the SSH simulations, $N_{wat}$ is distributed asymmetrically around 22, while the remaining simulations, with and without regulatory ions, sampled values distributed

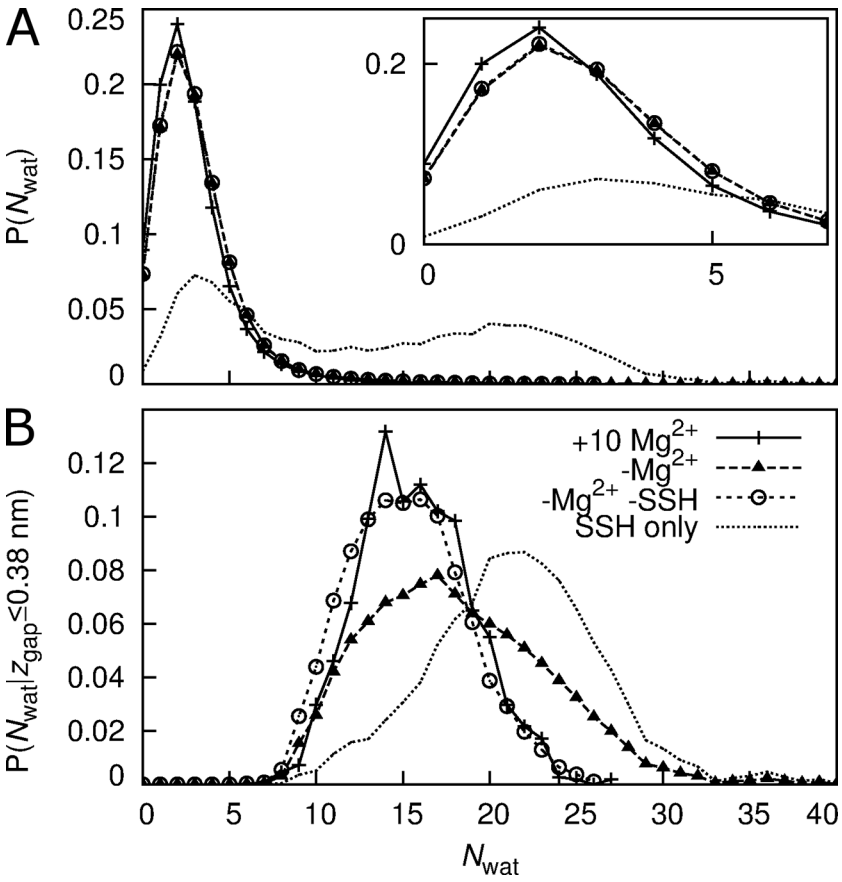


**Fig 6. Distribution of $N_{wat}$ in the MM.** (A) all conformations and (B) only those conformations with a wetted MM; for systems (plus symbols and solid line) with regulatory ions and (filled triangles and broken line) without regulatory ions. Dotted line represents this probability for the entire duration of the 8 simulations that sampled SSH states. Empty circles and dashed line represents this probability for the system without regulatory ions after removing the simulations that sampled SSH states from the analysis.

doi:10.1371/journal.pcbi.1004303.g006

normally around 15 (σ = 3). Thus, in the wet state, the dependence of the extent of hydration on regulatory ions was entirely due to the eight SSH simulations.

## Hydrophobic Wetting Kinetics

To characterize the kinetics of wetting and dewetting of the hydrophobic MM, survival probabilities, $S(t)$, were computed separately for wet and dry states, either with or without regulatory ions (Fig 7). Although wet states are more stable in the absence of regulatory ions, the difference between survival probabilities obtained with and without regulatory ions is abrogated by removing the SSH simulations from this analysis (Fig 7A). Thus, an essential difference between the two sets of simulations is that removal of the regulatory ions led to a hydration state not observed on the 35-ns time-scale in the presence of regulatory ions. The two wetted states differ both in the extent of hydration and in their kinetic properties. Conversely, the dewetted state of the MM was destabilized by the removal of regulatory ions, an effect that persists after removing the SSH simulations from this analysis (Fig 7B).

The survival probabilities of the wetted and dewetted MM states were fit to a double exponential decay function from which we computed the rate of channel wetting to be $8.2\times10^6 \pm 7\times10^5$ $s^{-1}$ and $4.1\times10^6 \pm 3\times10^5$ $s^{-1}$ in the absence and presence of regulatory ions, respectively (S1 Table). The estimates of wetting and dewetting rates were used to compute free energy differences between hydrated and dehydrated states (S2 Table), which we used to construct a model of hydrophobic gating in CorA (see Discussion).

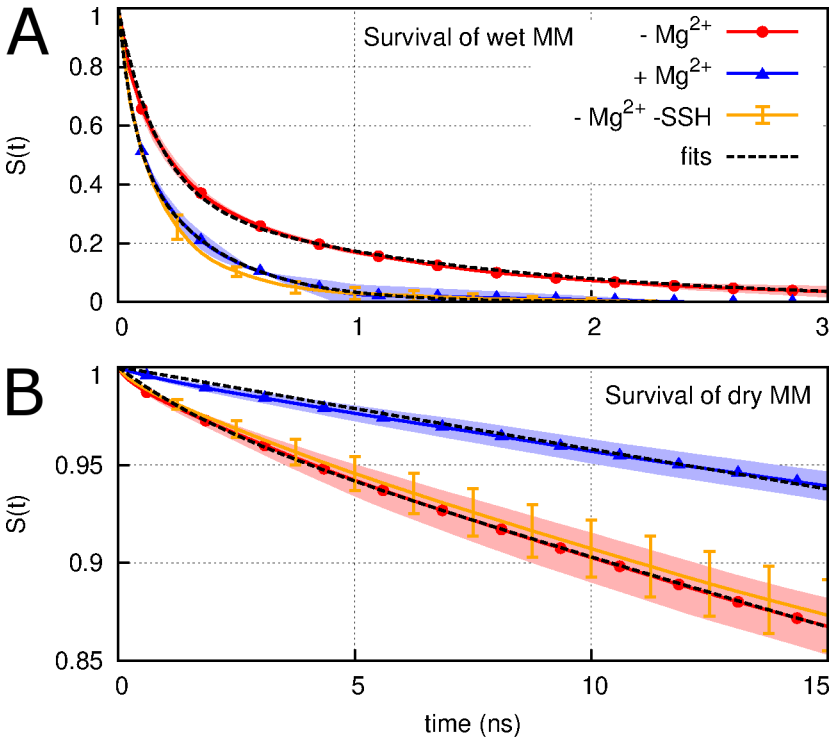


**Fig 7. Survival probabilities.** (A) completely connected water columns and (B) partial dehydration in the MM; for systems (blue line) with regulatory ions and (red line) without regulatory ions. The orange line was computed for the system without regulatory ions after removing the simulations that sampled SSH states from the analysis. Error estimates are the standard deviations obtained after dividing each set of 700 simulations into two groups.

doi:10.1371/journal.pcbi.1004303.g007

## Energetics of Magnesium Permeation

To assess whether the dilation and hydration of the hydrophobic stretch led to the open state of the channel, we used umbrella sampling (US) [33, 34] to compute the free energy associated with translocation of a divalent cation throughout the pore of TmCorA based on multiple starting conformations from each of four distinct states. These states correspond to hydrated and dehydrated MM with and without regulatory ions. Strictly speaking, our US simulations were conducted out of equilibrium since the channel conformation is slowly relaxing (S9 Fig). As such, these profiles provide estimates of the work required for ion permeation given initial states of protein conformation, pore hydration, and regulatory ion occupancy. Multiple free energy profiles from each state are shown together as ensemble averages in Fig 8. The general features of these profiles are similar: a small barrier at $z = 2.6$ nm, where the sidechain of N314 partially occludes the pore; a barrier of variable magnitude between $-1<z<1$ nm, which corresponds to the MM; a smaller barrier at $z = -2.3$ nm, which corresponds to the LC; and a minimum at $z = -3$ nm, which corresponds to the lower of two pore $Mg^{2+}$ binding sites.

The main difference between the four ensemble-averaged free energy profiles shown in Fig 8 is the height of the barrier in the MM. When the MM is fully dehydrated, it presents a very large barrier of 45±5 kcal/mol irrespective of regulatory binding site occupancy (Fig 8). The size of this barrier reduced to 25±5 kcal/mol when the MM was wetted, again irrespective of bound regulatory ions (Fig 8). Thus, the size of the free energy barrier in the MM correlates with its hydration and not with the presence of regulatory ions. This conclusion is supported and clarified by Fig 9, in which the magnitude of the free energy barrier in the MM, $\Delta G^{\ddagger}$, is plotted against values of $N_{wat}$ from initial US conformations, $N_{wat}(t_0)$, or $N_{wat}$(US), the average value of $N_{wat}$ from US simulations while the lumenal $Mg^{2+}$ ion was in the MM. The magnitude of $\Delta G^{\ddagger}$ is anticorrelated with both $N_{wat}(t_0)$ and $N_{wat}$(US) (Fig 9). Linear fits to all data yield $\Delta G^{\ddagger} = 46–0.82\times N_{wat}(t_0)$ kcal/mol and $\Delta G^{\ddagger} = 92–1.82\times N_{wat}$(US) kcal/mol, with $r^2$ coefficients of 0.80 and 0.83 respectively. By extrapolating these linear relationships, we predict that reducing the magnitude of the barrier to $\Delta G^{\ddagger} = 0$ kcal/mol requires 56 or 50 water molecules based on

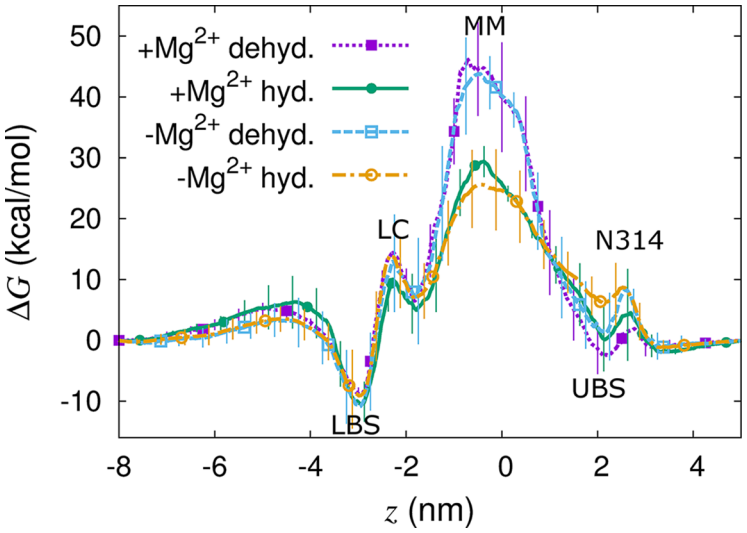


**Fig 8. Free energy profiles for a hexahydrated divalent cation through the TmCorA pore.** Profiles are shown for conformations in which the MM is (lines with circles) hydrated or (lines with squares) dehydrated, drawn from systems (dotted and solid lines) with regulatory ions and (dash and dash-dot lines) without regulatory ions. The center of mass of backbone atoms in the MM is at $z = 0$ nm. Error estimates are the standard deviation from repeated simulation using different starting conformations.

doi:10.1371/journal.pcbi.1004303.g008

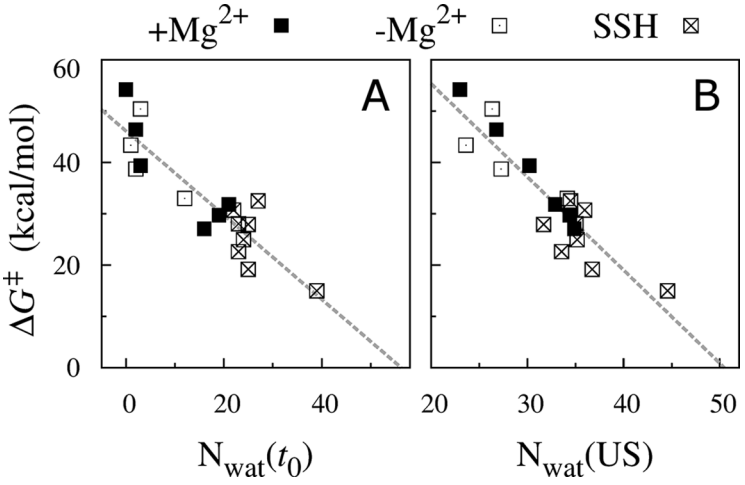


**Fig 9. Hydration of the MM is inversely correlated to the work required to move an ion from bulk water to the MM, $\Delta G^{\ddagger}$, irrespective of the presence of regulatory ions.** $\Delta G^{\ddagger}$ is shown as a function of (A) $N_{wat}$ from initial US conformations, $N_{wat}(t_0)$, or (B) the average value of $N_{wat}$ from production US while the lumenal $Mg^{2+}$ ion was in the MM, $N_{wat}$(US). Data from free energy profiles obtained (filled squares) with and (open squares) without regulatory ions. SSH simulations are identified by an x. Linear fits are indicated by dashed lines. Profiles of $N_{wat}$ as functions of lumenal $Mg^{2+}$ position are shown in S10 Fig.

doi:10.1371/journal.pcbi.1004303.g009

the two above equations, respectively. A linear fit of the relation between average MM pore diameter, $\overline{d_{pore}}$, and $N_{wat}$ in the absence of regulatory ions (Fig 5B), $\overline{d_{pore}} = 0.37+0.0067\times N_{wat}$ nm, suggests that the aforementioned values of $N_{wat}$ correspond to average pore diameters of 0.71 to 0.75 nm, slightly larger than the 0.68 nm diameter of hexahydrated $Mg^{2+}$. In turn, this result suggests that the barrier at the MM gate is essentially due to $Mg^{2+}$ desolvation, including effects beyond its first hydration shell. Note that the predicted diameter at which the gating barrier vanishes is significantly smaller than the ~1.2 nm diameter of the putative open state proposed by Dalmas *et al.* [28]. Furthermore, note that the requirement $\Delta G^{\ddagger} = 0$ is excessive as the channel may conduct $Mg^{2+}$ ions with moderate positive values of $\Delta G^{\ddagger}$. According to the model we present above, a pore diameter equal to that of hexahydrated $Mg^{2+}$ corresponds to $N_{wat} = 46$ and $\Delta G^{\ddagger} = 8$ kcal/mol.

## Single-Point Mutation Increasing MM Pore-Width

Because pore hydration reduces the free energy barrier to $Mg^{2+}$ flux, we assessed whether removing a (pentameric) bulky hydrophobic sidechain from the MM enhances its hydration. To this end, we conducted two-hundred 4-ns simulations for wild type and L294A TmCorA in three different wetted conformations extracted from our initial set of fourteen-hundred simulations. Consistent with the role of the MM as a hydrophobic gate, the L294A mutation enhances pore hydration both in the presence and in the absence of regulatory ions (Fig 10). In the presence of regulatory ions, L294A simulations initiated with $N_{wat} = 25$ stabilized at $N_{wat} = 32$ ($\sigma = 4$) over the last 3 ns (Fig 10C). Using the linear fit of $N_{wat}(t_0)$ to $\Delta G^{\ddagger}$ derived above, we predict that the pore remains closed to $Mg^{2+}$, with $\Delta G^{\ddagger} = 20$ kcal/mol. Therefore, even with the L294A mutation, further conformational rearrangement is required to attain an open state in the presence of regulatory ions. Similarly, wild type simulations initiated with $N_{wat} = 25$ or 42 remained stably hydrated with $N_{wat} = 24$ ($\sigma = 5$) or spontaneously became less hydrated until $N_{wat} = 32$ ($\sigma = 7$) at 4 ns, respectively (Fig 10A and 10B). Conversely, L294A simulations initiated with $N_{wat} = 25$ or 42 approached $N_{wat}$ values of 37 and 45, respectively ($\sigma = 5$; Fig 10A and 10B).

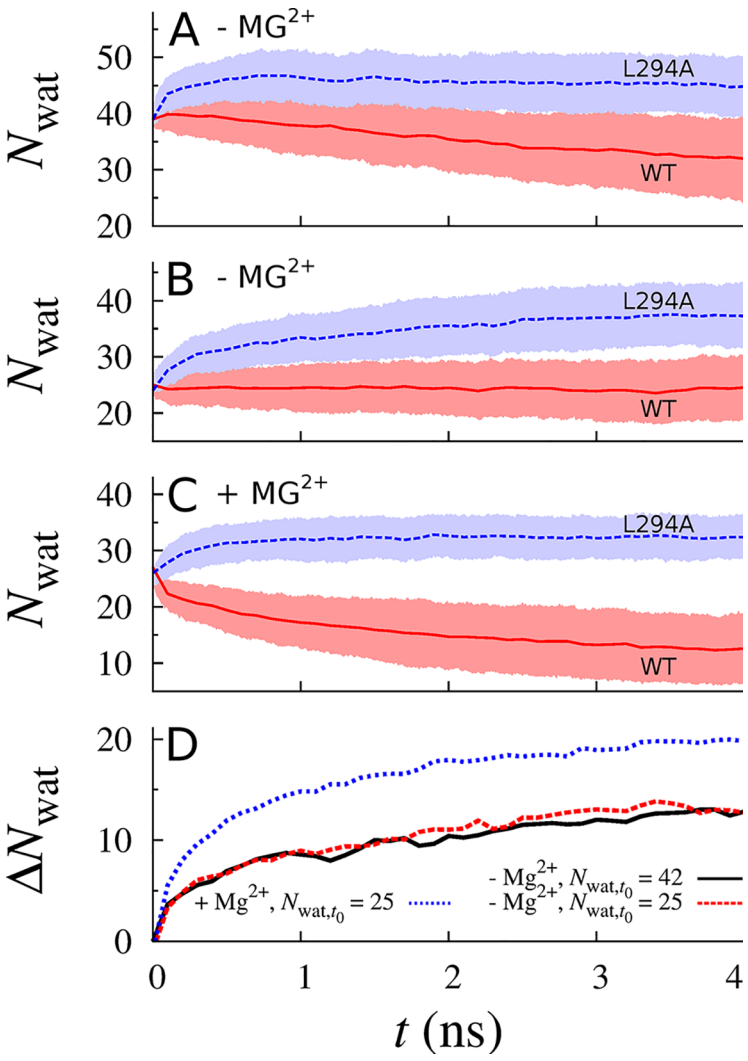


**Fig 10. Enhanced MM wetting resulting from pore-widening mutation L294A.** (A-C) Ensemble averages of the number of water molecules in the MM, $N_{wat}$, as functions of time, $t$, for (solid red) wild type, WT, and (broken blue) L294A simulations (A,B) without and (C) with regulatory ions in the DCS. Shaded regions enclose the standard deviation among 200 repeat simulations. Initial conformations had $N_{wat}$ values of (A) 42 or (B, C) 25. (D) Increase in hydration due to the L294A mutation, $\Delta N_{wat} = N_{wat}(L294A) — N_{wat}(WT)$, as a function of $t$ (black solid line) without regulatory ions, initial $N_{wat} = 42$; (red broken line) without regulatory ions, initial $N_{wat} = 25$; and (blue dotted line) with regulatory ions, initial $N_{wat} = 25$.

doi:10.1371/journal.pcbi.1004303.g010

Although these extents of hydration predict $\Delta G^{\ddagger}$ values between 9 and 16 kcal/mol, the standard deviations of five water molecules among our two-hundred repeat simulations indicates that ~33 simulations initiated with $N_{wat} = 42$ continued to sample values of $N_{wat}$ greater than 50 after 4 ns of simulation, and thus are predicted to present a barrier to $Mg^{2+}$ flux of only 5 kcal/mol. Therefore, in the absence of regulatory ions, the conformational changes that we observe in TmCorA may be sufficient to permit pore opening in the L294A mutant.

## Allosteric Gating Mechanism

We previously proposed that the unbinding of regulatory ions induces changes in the arrangement of protomers in the cytosolic domain of TmCorA which increases the probability of

hydration of the MM due to allosteric coupling via the long kinked and tilted helices that wrap around the pore in an iris-like fashion [29]. The present work confirms these conformational changes. Specifically, removing all ten regulatory $Mg^{2+}$ ions results in increased separation between the centers of mass of adjacent $Mg^{2+}$ binding domains (S11A Fig) and decreases the radial tilt angle of the intracellular region of helix 7 (S11B Fig), which together define the width of the funnel-like cytosolic domain. In addition, both the pore radius and the lateral tilt of helix 7 in the MM region increase upon removing regulatory $Mg^{2+}$ ions and further increase in the SSH runs (S11C and S11D Fig).

The first link in this allosteric mechanism is demonstrated by a clear correlation between fluctuations in $Mg^{2+}$ binding domain arrangement and changes in the radial tilt of the pore helices; although this correlation exists regardless of regulatory $Mg^{2+}$ occupancy, these structural fluctuations reach larger amplitudes when the regulatory sites are empty (S12A and S12E and S12I Fig). At the other end of the allosteric transmission, pore diameter and hydration are strongly correlated in the SSH simulations (S12J and S13B Figs), consistent with the above analysis (Fig 5). However, the allosteric mechanism by which we previously proposed radial tilt to cause pore dilation [29] was not strictly maintained throughout our new set of simulations. Specifically, the statistical linkage between average helix tilts and pore diameter is weak when all the SSH runs are considered together (S12L and S12K Fig) and only three out of eight SSH simulations show a significant correlation between average radial and lateral tilts of the pore helices (as defined by a Pearson coefficient magnitude above 0.4; see labels d, e, and h in S13C Fig). Furthermore, our previous description of the iris mechanism [29] involved a positive correlation between average radial and lateral tilts, whereas this correlation is negative in two of the SSH simulations (see labels d and e in S13C Fig), indicating that both increases and decreases in radial tilt of the cytosolic region of helix 7 can lead to pore dilation.

A crystal structure of TmCorA recently obtained in the absence of divalent cations suggests that protomeric asymmetry involving bending of the intracellular domain with respect to the transmembrane region is a precondition for channel opening [14]. Accordingly, the analysis of our simulations shows that asymmetric stalk-helix bending is enhanced by the removal of regulatory ions (S14 Fig). However, there is no correlation between stalk-helix bending and the hydration of the hydrophobic gate (S15 and S16 Figs), suggesting that our 35-ns simulations sample early stages of pore wetting and dilation, and that longer timescales are required for full channel opening.

## Discussion

Like a previous simulation study of protein folding kinetics [35], this study exploited the fact that rare events can be observed from massively-repeated short time trajectories provided that the simulation time exceeds the minimum passage time through the transition state. Our simulations were long enough for wetting and dewetting of the channel to occur, and the number of repeats was large enough to observe hundreds of such transitions, allowing us to derive quantitative estimates of wetting and dewetting kinetics.

Significantly, the MM became hydrated more often when regulatory ions were absent from the simulations (Fig 2). Experimentally, Payandeh *et al*. have shown that a D253F mutation in one of the two pentameric regulatory binding sites enhances bacterial growth in limiting $Mg^{2+}$ conditions [17], presumably because it reduces the ability of these sites to bind $Mg^{2+}$, preventing closure of TmCorA. More recently, Dalmas *et al*. have shown that a D253K mutation abolishes current regulation by the DCS [28]. In addition, our finding that regulatory ions affect hydration of the MM, but not the LC (Figs 2 and 7), suggests that it is the former that is allosterically controlled by regulatory ions in early wetting. However, structural models of the open

state generated by Dalmas *et al*. based on spectroscopic data predict an increased pore diameter throughout the entire channel lumen [28], suggesting that longer-timescale pore opening events involve dilation of the LC. In this context, it remains unclear why a pore-widening mutation at the LC (L280A) compromises bacterial growth in limiting $Mg^{2+}$ conditions [17].

The magnitude of the free energy barrier in the MM decreased as it became more hydrated (Fig 9). Consistent with this finding, mutations that shorten the sidechain of MM residue L294 enhance bacterial growth in limiting $Mg^{2+}$ conditions [17, 18] and L294A increases the rate of liposomal uptake of $Mg^{2+}$ by 2.5-fold in a fluorescence-based flux assay [17]. Simulations of the L294A mutant confirm its increased propensity for MM wetting (Fig 10) and suggest that the largest widening of the TmCorA pore observed in our simulations may be sufficient to permit $Mg^{2+}$ flux in the L294A mutant. Our results suggest that these mutations enhance channel activity by increasing the water-accessible volume of the MM region, leading to increased hydration and thereby decreasing the barrier to $Mg^{2+}$ flux.

Hydrophobic gating has been discussed extensively in the literature [36–44]. The transient, reversible wetting of the MM revealed in our simulations (Fig 7) is consistent with the concept that water molecules near hydrophobic surfaces are close to a vapor-to-liquid phase transition [45]. Hydrophobic surfaces alter the phase behavior of water [46], especially when it is tightly confined [31], and wetting equilibria can be dramatically altered by subtle changes in hydrophobicity [32]. Specifically, hydrophobic surfaces enhance water density fluctuations in their vicinity [45, 47], thereby increasing the probability of cavity formation [47]. When such a cavity spans the gap between hydrophobic surfaces, it can nucleate the formation of a vapor phase [31] via capillary drying [48]. Taken together, the above findings suggest that the hydrophobic gate of TmCorA is poised near the edge of a wetting/dewetting transition that can be pushed toward wetting by a single (pentameric) L→A or L→G mutation. Analogous roles have been ascribed to a single (hexameric) V→A mutation in the hydrophobic bottleneck of a calcium release-activated calcium channel [49] and a single I→G mutation that affects the wetting of hydrophobic surfaces during melittin dimerization [45]. In the present study, condensation of water in the MM was correlated to small-amplitude dilations of the pore-lining helices (Figs 4 and 5, S12B, S12F, and S12J Fig). Apolar surfaces only dry when they are sufficiently large [46] and capillary dehydration occurs more rapidly when the enclosing apolar surfaces are closer and longer [31]. At a modal length of 1.9 nm (S2B and S2F Fig) and lumenal diameter on the order of 0.4–0.6 nm (Fig 5), with an average helical spread of 1.54 nm (S12C and S12G Fig), the hydrophobic MM appears to be well constructed to employ capillary dehydration as a gating mechanism.

We observed the following three distinct hydration states in the MM: First, the majority of our simulations remained in a dry state. Second, a wetted state of low hydration, characterized by an average $\overline{N_{Wat}} = 15$ ($\sigma = 3$), was transiently populated and occurred more often when regulatory ions were absent (Table 1 and Fig 7B and S2 Fig). Although the opening rate of TmCorA is unknown experimentally, the observed rate of wetting in our simulations, $8.2\times10^6 \pm 7\times10^5$ $s^{-1}$ (S1 Table), is 100–1,000 times faster than the opening rate of any known ion channel, including those involved in fast excitatory neurotransmission such as nicotinic acetylcholine receptors ($1\times10^4$ to $8\times10^4$ $s^{-1}$) [50, 51] and AMPA glutamate receptors ($7\times10^4$ to $8\times10^4$ $s^{-1}$) [52, 53]. Thus, together with the fact that this transient hydrated state is impermeable to $Mg^{2+}$ (Figs 8 and 9), the high rate of wetting suggests that this state is an intermediate. Finally, the third state that we identified, the SSH state (Fig 4 and S4 Fig), differed from transiently-hydrated states in terms of the extent and duration of hydration and in that it was not observed in the presence of regulatory ions (Figs 3, 6 and 7 and S6 Fig).

The overall effect of removing regulatory ions was to increase the extent of hydration in the MM and to increase the stability of wetted states. We propose the following model of wetting

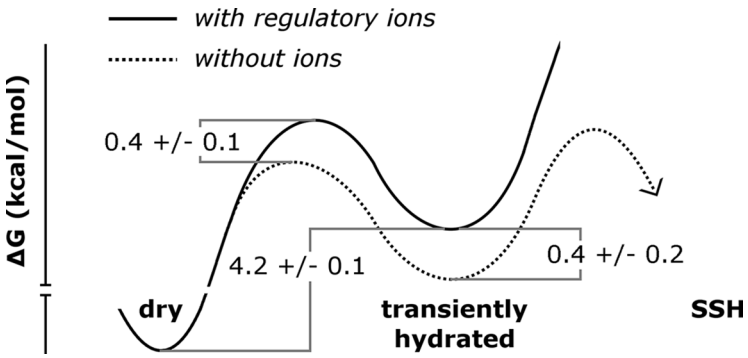


**Fig 11. A model of hydrophobic gating in TmCorA.**

doi:10.1371/journal.pcbi.1004303.g011

and dewetting transitions in the MM, as depicted in Fig 11. In the presence of regulatory ions, the dry state is favored over the transiently hydrated state by 4.2 ± 0.1 kcal/mol (S2 Table). When regulatory ions are removed, the free energy of the transiently-hydrated state, and the barrier to hydration, are reduced by 0.4 ± 0.2 kcal/mol. Regulatory ions thus modulate the rate of wetting but not dewetting transitions respectively to and from the transiently-hydrated state. Furthermore, transitions to the SSH state only occurred in the absence of regulatory ions (Figs 3, 6 and 7, and S6 Fig). This result, together with the linear increase in MM wetting with time (Fig 2A), indicates that equilibrium has not been reached in the absence of regulatory ions and that longer simulations would lead to increasingly divergent fractions of MM wetting based on regulatory ion occupancy.

The steepness of the drop in $\Delta G^{\ddagger}$ vs. the extent of hydration, which was observed both with and without regulatory ions (Figs 8 and 9), indicates switch-like behavior. We hypothesize that the removal of regulatory ions stabilizes the SSH state much more dramatically than it stabilizes transiently hydrated states and that the SSH state plays an important role in TmCorA's gating mechanism. Extrapolation of the relationship between $\Delta G^{\ddagger}$ and $N_{wat}$ suggests that the channel may open to divalent cation flux when more than ~50 water molecules condense in the MM.

Using large-scale sampling, we have characterized the mechanism and kinetics of wetting and dewetting transitions in a 1.9-nm-long hydrophobic constriction of the magnesium channel CorA. Massively-repeated simulations reveal essential differences in the dynamic fluctuations and relaxation of this hydrophobic gate in response to the removal of regulatory ions more than 6 nm away. The analysis of rate constants for wetting and dewetting transitions and of free energy profiles of ionic permittivity indicates that the hydrated states observed in the present study are intermediate states rather than the open state of the channel. These results lead to a model of functional gating of CorA in which regulatory ions control pore hydration, which in turn controls the onset of ionic conduction. A key event underpinning this allosteric mechanism, wetting constitutes a requisite but not sufficient step towards channel opening, as it is the extent of hydration of the pore, not the presence of water *per se*, that determines the barrier to ion permeation. Taken together, these findings demonstrate how capillary wetting transitions help mediate robust, non-linear switching of ionic conduction and underline the relevance of hydrophobic gating to ion channel structure and function.

## Methods

The simulation systems consisted of TmCorA [13], with and without 10 regulatory $Mg^{2+}$ ions in the DCS, in a hydrated 1,2-dimyristoyl-*sn*-glycero-3-phosphatidylcholine (DMPC) bilayer.

This system comprised 250,000 atoms. Simulations were performed with GROMACS [54]. The water model was TIP3P [55]. TmCorA was modeled by the OPLS-AA/L parameters [56, 57]. DMPC was modeled by the Berger parameters [58] using the half-ε double-pairlist method [29]. The $Mg^{2+}$ parameters were those of Åqvist [59]. For additional details of system setup and massively repeated simulation, and for a description of the algorithms that we used to quantify hydration, see S2 Text.

To evaluate the free energy profile for the permeation of a divalent cation throughout the pore of TmCorA, we used umbrella sampling (US) MD simulations [33, 34]. In these simulations, we inserted hexahydrated magnesium into the pore, instead of a naked ion, because interactions between magnesium and water molecules in its first hydration shell are very strong [60], suggesting that magnesium is hexahydrated throughout a large part of the conduction pathway. We conducted 261 2-ns simulations in which the axial position of the magnesium ion relative to the center of mass of the hydrophobic gate, $z$, was harmonically restrained to a specified value, $z_i^0$, for restraining potentials (umbrellas), $i$, distributed every 0.05 nm in the range $-8 \leq z_i^0 \leq 5$ nm. These 261 simulations constituted one set of US simulations and were used to generate one evaluation of the free energy profile. Altogether, we conducted 18 sets of US simulations, providing 18 independent evaluations of the free energy profile. In so doing, we computed free energy profiles for four different conformational basins of the TmCorA system, all drawn from our massively repeated sampling. The four basins were: those with the largest and smallest values of $N_{wat}$ in the MM, obtained either in the presence or absence of regulatory ions. For each basin, we conducted 3 sets of US simulations, each using a different conformation extracted from a different simulation, except for the large-$N_{wat}$ state in the absence of regulatory ions, for which 9 distinct conformations of TmCorA were used to compute 9 free energy profiles. For additional details, see S2 Text.

## Supporting Information

**S1 Text. Supplementary Results investigate the possibility of pore reorganization involving the exposure of hydrophilic moieties to the pore lumen.**
(PDF)

**S2 Text. Supplementary Methods provide detailed descriptions of system setup, massively repeated and umbrella sampling simulations, and algorithms used to quantify hydration.**
(PDF)

**S1 Table. Exponential decay fitting parameters and integrals for profiles of survival probabilities, $S(t)$.** Fits are shown separately for (A) the first 350 simulations and (B) the second 350 simulations. (C) Mean lifetime, $\tau$. (D) Mean half-life, $t_{1/2}$. (E) First-order rate constant, $k$. (n.c. stands for not computed).
(PDF)

**S2 Table. Free energy values obtained from ratios of the integrals provided in S1 Table.** Here, d→tw indicates a transition from the dry state to the transiently wet state.
(PDF)

**S1 Fig. A snapshot in which a water column transiently connected the interior of the MM to bulk water on the cytoplasmic side of the bilayer.** The bilayer is depicted in spheres for (white) carbon, (red) oxygen, (blue) nitrogen, and (brown) phosphorus atoms. Water molecules are shown in cyan. TmCorA is depicted as grey ribbons. Methionine and leucine side chains are shown as yellow and orange sticks, respectively.
(TIF)

**S2 Fig. Distributions of the two hydration metrics $N_{wat}$ and $z_{gap}$ in simulations (A-D) without regulatory ions and (E-H) with regulatory ions.** (A and E) Contour plots correlating $N_{wat}$ and $z_{gap}$ (Pearson correlation coefficient of -0.8). (B and F) The probability profile of $z_{gap}$, in which local minimum at $z_{gap}$ = 0.38 nm is indicated by a horizontal line. (C and G) The probability profile of $N_{wat}$. In parts B,C,F, and G, both (dashed line) linear- and (solid line) log-scale probabilities are shown, offset for clarity. (*) In part C, probabilities of $N_{wat}$ remain non-zero beyond the edge of the plot. (D and H) Inset contour maps of the location of the center of the local dehydration along **z** with respect to the center of mass of the MM, $z_{gap}^{center}$, as a function of the length of the dehydrated region. Dotted lines enclose one standard deviation of the positions of the $C_\alpha$ atoms of M291 and M302, the residues which bound the MM.
(TIF)

**S3 Fig. Distributions of the hydration metric $z_{gap}$ in the MM and LC for systems (A-C) without regulatory ions and (D-F) with regulatory ions.** (A and D) Contour plots correlating $z_{gap}$ values in the MM and LC. (B and E) The probability profile of $z_{gap}$ in the MM. (C and F) The probability profile of $z_{gap}$ in the LC. Both (dashed line) linear- and (solid line) log-scale probabilities are shown in parts B,C,E, and F, offset for clarity. A local minimum at $z_{gap}$ = 0.38 nm is indicated by horizontal and vertical dotted lines.
(TIF)

**S4 Fig. Time series of pore hydration in the SSH simulations without $Mg^{2+}$.** The number of water molecules in the MM, $N_{wat}$, and the length of the largest dehydration, $z_{gap}$, are shown. The eight SSH trajectories are ordered A to H by decreasing percent of time spent with $N_{wat} > 20$.
(TIF)

**S5 Fig. Time series of pore hydration in selected simulations without $Mg^{2+}$.** The number of water molecules in the MM, $N_{wat}$, and the length of the largest dehydration stretch, $z_{gap}$ (nm) are shown. Simulations are ordered by decreasing time spent with $N_{wat} > 10$ and trajectories are shown from the (A) 98$^{th}$, (B) 95$^{th}$, (C) 90$^{th}$, and (D) 50$^{th}$ percentile.
(TIF)

**S6 Fig. Time series of pore hydration in selected simulations with $Mg^{2+}$.** The number of water molecules in the MM, $N_{wat}$, and the length of the largest dehydration stretch, $z_{gap}$ (nm) are shown for (A-D) the four simulations with the largest time spent with $N_{wat} > 10$ and (E-H) representative trajectories at the 98$^{th}$, 95$^{th}$, 90$^{th}$, and 50$^{th}$ percentile.
(TIF)

**S7 Fig. Analysis of lumen-facing groups and pore-water interactions in the MM region.** (A-D) Dependence of the number of hydrogen bonds between MM residues and lumenal water molecules, $N_{H\text{-}bond}$, upon the number of water molecules in the MM, $N_{wat}$, successively (A, B) without and (C, D) with regulatory magnesium ions. (B, D) Insets show the average value of $N_{H\text{-}bond}$ as a function of $N_{wat}$. (E) Extracellular view of TmCorA showing the snapshot with the largest observed value of $N_{H\text{-}bond}$ = 7 (not a SSH simulation). Water molecules in the MM that do not engage in water-protein hydrogen bonding are depicted with thinner lines. (F) Orientation of polar backbone groups and side chains of the MM relative to the pore: probability distributions of the (red) backbone O-C-$C_{COM}$ angle; (blue) backbone H-N-$N_{COM}$ angle; (black) lysine $N_\zeta$-$C_\alpha$-$C_{\alpha COM}$ angle; and (green) threonine O$\gamma$-$C_\alpha$-$C_{\alpha COM}$ angle (in this notation, the subscript $_{COM}$ indicates the center of mass of the five protomeric atoms at a given location). Solid and patterned lines denote simulations without and with regulatory ions, respectively. The appropriate vectors are computed for all MM residues (M291-M302) on all five protomers and combined into a single histogram. (G, H) View of

the MM and its hydration from simulations without regulatory magnesium ions in which the carbonyl oxygen atom of F301 accesses the pore, showing snapshots from the (G) least and (H) most hydrated such simulations. MM methionine $S_\delta$ atoms are shown as yellow spheres and the F301 C = O atoms are shown as cyan and red spheres, respectively. The protein's MM is shown as a cartoon with a colored surface.
(TIF)

**S8 Fig. Pore reorganization predominantly involves an increase in volume, not in hydrophilic exposure.** (A-C) Snapshots depict the (left) least and (right) most hydrated simulation without regulatory ions depicting (A) hydrophilic backbone groups, (B) hydrophilic side chains, and (C) hydrophobic side chains along the MM. (D) Probability that the backbone (red) CO or (blue) NH bond vectors project into the pore (angle $\leq 40°$ as defined in the caption of S7 Fig) as a function of $N_{wat}$.
(TIF)

**S9 Fig. Convergence of PMFs for ionic conduction.** Sampling was initiated using a structure in which the MM was initially (A) wet or (B) dry. Neither of these systems contained regulatory ions. In each case, four PMFs are shown, each computed from 1 ns of sampling per umbrella after an increasing amount of equilibration time per umbrella, $t_{eq}$, which was either (solid line) 0, (long-dashed line) 1, (short-dashed line) 9, or (dotted line) 19 ns. (C) The magnitude of the free energy barrier in the MM is shown as a function of $t_{eq}$ for the systems in which the MM was initially ("x" symbols and broken line) wet or (open squares and solid line) dry.
(TIF)

**S10 Fig. Hydration of the MM in US simulations.** Each plot depicts a set of US simulations initiated with a different starting structure. Dashed blue horizontal lines indicate the number of water molecules initially in the MM. The average values of $N_{wat}$ sampled during US simulations are shown as functions of the position of the lumenal $Mg^{2+}$ ion along the pore axis, $z$, which is centered at the center of mass of MM backbone atoms. Values of $N_{wat}$ are averaged over the (red circles) first or (black lines) second ns of simulation/umbrella. Note that the ordinate, $N_{wat}$, describes hydration of the MM and not the local environment around the lumenal $Mg^{2+}$ ion.
(TIF)

**S11 Fig. Dependence of channel structure on the presence of regulatory $Mg^{2+}$.** Data are shown for (dotted black line with filled triangles) all 700 simulations with regulatory ions, (dashed blue line with open circles) the 692 non-SSH simulations without regulatory ions, and (red solid line) the 8 SSH simulations identified in Fig 3 for the system with no regulatory ions. Probability distributions of (A) distances between the centers of mass of adjacent cytoplasmic domains, $d_{MBD}$, (B) radial tilts of the cytoplasmic part of the pore-lining helices, $= "OT7d6df7ab_l"\theta^{IC}_{Rad}$, (C) lateral tilts of α7 helices on the pore surface in the MM, $\theta^{MM}_{Lat}$, and (D) distances of the axes of α7 helices from the center of the pore in the MM, $d^{MM}_{center}$.
(TIF)

**S12 Fig. Dependence of structural fluctuations of the channel on the presence of regulatory $Mg^{2+}$.** Data are shown for (A-D) all 700 simulations with regulatory ions, (E-H) all 700 simulations without regulatory ions, and (I-L) the 8 stably superhydrated (SSH) simulations identified in Fig 3 for the system with no regulatory ions. Symbols are the same as those in S11 Fig, except that here bars over symbols denote average values from the five protomers. Pairwise correlations are shown for (A,E,I) $\overline{\theta^{IC}_{Rad}}$ *vs* $\overline{d_{MBD}}$, (B,F,J) $\overline{d^{MM}_{center}}$ *vs* $N_{wat}$, (C,G,K) $\overline{\theta^{IC}_{Rad}}$ *vs* $\overline{\theta^{MM}_{Lat}}$, and

(D,H,L) $\overline{d^{MM}_{center}}$ *vs* $\overline{\theta^{MM}_{Lat}}$. Regions of dense sampling are colored blue and regions of sparse sampling are colored yellow.
(TIF)

**S13 Fig. Probability distributions of the Pearson correlation coefficients of channel structure and hydration.** Pearson coefficients, $\rho$, were computed from individual simulations for the four pairs of metrics considered in S12 Fig. Distributions are shown for (solid line) all 700 simulations without regulatory ions and (broken line) all 700 simulations with regulatory ions. The Pearson correlation coefficient of each of the 8 stably superhydrated simulations is identified in each plot by vertical lines and the letters a-h, which correspond to simulation identifiers in S4 Fig. SSH identifiers are distributed along the ordinate to ease reading, but only contain information in relation to the abscissa.
(TIF)

**S14 Fig. Stalk helix bending with and without regulatory ions.** Probability histograms of the instantaneous (A) minimum, (B) average, and (C) root mean squared deviation (RMSD) of the bending angle between V248, L280, and I310 (all $C_\alpha$) in each protomer for simulations conducted (dashed red lines) with and (solid black lines) without regulatory ions. Standard deviations were obtained by dividing each set of 700 simulations into 2 subsets.
(TIF)

**S15 Fig. Stalk helix bending without regulatory ions.** Probability histograms of the instantaneous (A) minimum, (B) average, and (C) root mean squared deviation (RMSD) of the bending angle between V248, L280, and I310 (all $C_\alpha$) in each protomer for (solid black lines) all simulations, (dotted red line) not including the SSH simulations, and (dashed blue line) only the SSH simulations. The dotted red line appears almost exactly on top of the solid black line.
(TIF)

**S16 Fig. Stalk helix bending without regulatory ions as a function of pore hydration.** Heat maps evaluate pore hydration via (A-C) $N_{wat}$ and (D-F) $z_{gap}$ and the instantaneous (A, D) minimum, (B, E) average, and (C, F) root mean squared deviation (RMSD) of the bending angle between V248, L280, and I310 (all $C_\alpha$) in each protomer.
(TIF)

**S1 Movie. Wetting of the hydrophobic gate of TmCorA during a selected 35-ns simulation.** Movie depicts TmCorA (grey ribbons) in a lipid bilayer (coloured sticks) and highlights pore hydration by luminal water molecules (yellow spheres). This trajectory represents the SSH simulation in which the MM contained the largest values of $N_{wat}$. It was conducted in the absence of regulatory ions.
(AVI)

## Acknowledgments

We thank Grace Li for computing Pearson correlation coefficients. Computations were performed at SciNet [61].

## Author Contributions

Conceived and designed the experiments: CN NC RP. Performed the experiments: CN NC. Analyzed the data: CN NC PP. Contributed reagents/materials/analysis tools: CN NC PP. Wrote the paper: CN EFP RP.

## References

1. Yang C-Y. Calcium and magnesium in drinking water and risk of death from cerebrovascular disease. Stroke. 1998; 29(2):411–4. PMID: 9472882
2. Rubenowitz E, Axelsson G, Rylander R. Magnesium in drinking water and death from acute myocardial infarction. Am J Epidemiol. 1996; 143(5):456–62. PMID: 8610660
3. Ueshima K. Magnesium and ischemic heart disease: a review of epidemiological, experimental, and clinical evidences. Magnesium Res. 2005; 18(4):275–84.
4. Kucharski LM, Lubbe WJ, Maguire ME. Cation hexaammines are selective and potent inhibitors of the CorA magnesium transport system. J Biol Chem. 2000; 275(22):16767–73. PMID: 10748031
5. Gouaux E, MacKinnon R. Principles of selective ion transport in channels and pumps. Science. 2005; 310(5753):1461–5. PMID: 16322449
6. Kehres DG, Lawyer CH, Maguire ME. The CorA magnesium transporter gene family. Microb Comp Genomics. 1998; 3(3):151–69. PMID: 9775386
7. Moomaw AS, Maguire ME. The unique nature of Mg2+ channels. Physiology. 2008; 23(5):275–85.
8. Dalmas O, Sandtner W, Medovoy D, Frezza L, Bezanilla F, Perozo E. A repulsion mechanism explains magnesium permeation and selectivity in CorA. P Natl Acad Sci USA. 2014; 111(8):3002–7.
9. Knoop V, Groth-Malonek M, Gebert M, Eifler K, Weyand K. Transport of magnesium and other divalent cations: evolution of the 2-TM-GxN proteins in the MIT superfamily. Mol Genet Genomics. 2005; 274 (3):205–16. PMID: 16179994
10. Bui DM, Gregan J, Jarosch E, Ragnini A, Schweyen RJ. The bacterial magnesium transporter CorA can functionally substitute for Its putative homologue Mrs2p in the yeast inner mitochondrial membrane. J Biol Chem. 1999; 274(29):20438–43. PMID: 10400670
11. Lunin VV, Dobrovetsky E, Khutoreskaya G, Zhang R, Joachimiak A, Doyle DA, et al. Crystal structure of the CorA Mg2+ transporter. Nature. 2006; 440(7085):833–7. PMID: 16598263
12. Eshaghi S, Niegowski D, Kohl A, Molina DM, Lesley SA, Nordlund P. Crystal structure of a divalent metal ion transporter CorA at 2.9 Angstrom resolution. Science. 2006; 313(5785):354–7. PMID: 16857941
13. Payandeh J, Pai EF. A structural basis for Mg2+ homeostasis and the CorA translocation cycle. EMBO J. 2006; 25(16):3762–73. PMID: 16902408
14. Pfoh R, Li A, Chakrabarti N, Payandeh J, Pomès R, Pai EF. Structural asymmetry in the magnesium channel CorA points to sequential allosteric regulation. P Natl Acad Sci USA. 2012; 109(46):18809–14.
15. Guskov A, Nordin N, Reynaud A, Engman H, Lundbäck A-K, Jong AJO, et al. Structural insights into the mechanisms of Mg2+ uptake, transport, and gating by CorA. P Natl Acad Sci USA. 2012; 109 (45):18459–64.
16. Nordin N, Guskov A, Phua T, Sahaf N, Xia Y, Lu S, et al. Exploring the structure and function of Thermotoga maritima CorA reveals the mechanism of gating and ion selectivity in Co2+/Mg2+ transport. Biochem J. 2013; 451(3):365–74. doi: 10.1042/BJ20121745 PMID: 23425532
17. Payandeh J, Li C, Ramjeesingh M, Poduch E, Bear CE, Pai EF. Probing structure-function relationships and gating mechanisms in the CorA mg2+ transport system. J Biol Chem. 2008; 283(17):11721–33. doi: 10.1074/jbc.M707889200 PMID: 18276588
18. Svidová S, Sponder G, Schweyen RJ, Djinović-Carugo K. Functional analysis of the conserved hydrophobic gate region of the magnesium transporter CorA. BBA-Biomembranes. 2011; 1808(6):1587–91. doi: 10.1016/j.bbamem.2010.10.017 PMID: 21074514
19. Miyazawa A, Fujiyoshi Y, Unwin N. Structure and gating mechanism of the acetylcholine receptor pore. Nature. 2003; 423(6943):949–55. PMID: 12827192
20. Zhu F, Hummer G. Pore opening and closing of a pentameric ligand-gated ion channel. P Natl Acad Sci USA. 2010; 107(46):19814–9.
21. Cheng X, Ivanov I, Wang H, Sine SM, McCammon JA. Molecular-dynamics simulations of ELIC—a prokaryotic homologue of the nicotinic acetylcholine receptor. Biophys J. 2009; 96(11):4502–13. doi: 10.1016/j.bpj.2009.03.018 PMID: 19486673
22. Zhu F, Hummer G. Drying transition in the hydrophobic gate of the GLIC channel blocks ion conduction. Biophys J. 2012; 103(2):219–27. doi: 10.1016/j.bpj.2012.06.003 PMID: 22853899
23. Jensen MØ, Borhani DW, Lindorff-Larsen K, Maragakis P, Jogini V, Eastwood MP, et al. Principles of conduction and hydrophobic gating in K+ channels. P Natl Acad Sci USA. 2010; 107(13):5833–8. 7.
24. Jensen MØ, Jogini V, Borhani DW, Leffler AE, Dror RO, Shaw DE. Mechanism of voltage gating in potassium channels. Science. 2012; 336(6078):229–33. doi: 10.1126/science.1216533 PMID: 22499946

25. Törnroth-Horsefield S, Wang Y, Hedfalk K, Johanson U, Karlsson M, Tajkhorshid E, et al. Structural mechanism of plant aquaporin gating. Nature. 2006; 439(7077):688–94. PMID: 16340961

26. Kung C, Martinac B, Sukharev S. Mechanosensitive channels in microbes. Annu Rev Microbiol. 2010; 64(1):313–29.

27. Anishkin A, Akitake B, Kamaraju K, Chiang CS, Sukharev S. Hydration properties of mechanosensitive channel pores define the energetics of gating. J Phys-Condens Mat. 2010; 22(45):454120.

28. Dalmas O, Sompornpisut P, Bezanilla F, Perozo E. Molecular mechanism of Mg2+-dependent gating in CorA. Nat Commun. 2014; 5.

29. Chakrabarti N, Neale C, Payandeh J, Pai EF, Pomès R. An iris-like mechanism of pore dilation in the CorA magnesium transport system. Biophys J. 2010; 98(5):784–92. doi: 10.1016/j.bpj.2009.11.009 PMID: 20197031

30. Palombo I, Daley DO, Rapp M. Why is the GMN motif conserved in the CorA/Mrs2/Alr1 superfamily of magnesium transport proteins? Biochemistry. 2013; 52(28):4842–7. doi: 10.1021/bi4007397 PMID: 23781956

31. Sharma S, Debenedetti PG. Evaporation rate of water in hydrophobic confinement. P Natl Acad Sci USA. 2012; 109(12):4365–70.

32. Hummer G, Rasaiah JC, Noworyta JP. Water conduction through the hydrophobic channel of a carbon nanotube. Nature. 2001; 414(6860):188–90. PMID: 11700553

33. Torrie GM, Valleau JP. Nonphysical sampling distributions in Monte Carlo free-energy estimation: umbrella sampling. J Comput Phys. 1977; 23(2):187–99.

34. Roux B. The calculation of the potential of mean force using computer simulations. Comput Phys Commun. 1995; 91(1–3):275–82.

35. Snow CD, Nguyen H, Pande VS, Gruebele M. Absolute comparison of simulated and experimental protein-folding dynamics. Nature. 2002; 420(6911):102–6. PMID: 12422224

36. Corry B. An energy-efficient gating mechanism in the acetylcholine receptor channel suggested by molecular and brownian dynamics. Biophys J. 2006; 90(3):799–810. PMID: 16284265

37. Beckstein O, Sansom MSP. A hydrophobic gate in an ion channel: the closed state of the nicotinic acetylcholine receptor. Physical Biology. 2006; 3(2):147. PMID: 16829701

38. Beckstein O, Biggin PC, Bond P, Bright JN, Domene C, Grottesi A, et al. Ion channel gating: insights via molecular simulations. FEBS Letters. 2003; 555(1):85–90. PMID: 14630324

39. Beckstein O, Biggin PC, Sansom MSP. A hydrophobic gating mechanism for nanopores. J Phys Chem B. 2001; 105(51):12902–5.

40. Beckstein O, Sansom MSP. The influence of geometry, surface character, and flexibility on the permeation of ions and water through biological pores. Phys Biol. 2004; 1(1):42.

41. Beckstein O, Tai K, Sansom MSP. Not ions alone: barriers to ion permeation in nanopores and channels. J Am Chem Soc. 2004; 126(45):14694–5. PMID: 15535674

42. Allen R, Melchionna S, Hansen J-P. Intermittent permeation of cylindrical nanopores by water. Phys Rev Lett. 2002; 89(17):175502. PMID: 12398681

43. Allen R, Hansen J-P, Melchionna S. Molecular dynamics investigation of water permeation through nanopores. J Chem Phys. 2003; 119(7):3905–19.

44. Allen R, Melchionna S, Hansen J-P. Permeation of nanopores by water: the effects of channel polarization. J Phys: Condens Matter. 2003; 15(1):S297.

45. Patel AJ, Varilly P, Jamadagni SN, Hagan MF, Chandler D, Garde S. Sitting at the edge: How biomolecules use hydrophobicity to tune their interactions and function. J Phys Chem B. 2012; 116(8):2498–503. doi: 10.1021/jp2107523 PMID: 22235927

46. Lum K, Chandler D, Weeks JD. Hydrophobicity at Small and Large Length Scales. J Phys Chem B. 1999; 103(22):4570–7. m.

47. Godawat R, Jamadagni SN, Garde S. Characterizing hydrophobicity of interfaces by using cavity formation, solute binding, and water correlations. Proceedings of the National Academy of Sciences. 2009; 106(36):15119–24.

48. Beckstein O, Sansom MSP. Liquid—vapor oscillations of water in hydrophobic nanopores. Proceedings of the National Academy of Sciences. 2003; 100(12):7063–8.

49. Dong H, Fiorin G, Carnevale V, Treptow W, Klein ML. Pore waters regulate ion permeation in a calcium release-activated calcium channel. P Natl Acad Sci USA. 2013; 110(43):17332–7.

50. Maconochie DJ, Steinbach JH. The channel opening rate of adult- and fetal-type mouse muscle nicotinic receptors activated by acetylcholine. J Physiol. 1998; 506(1):53–72.

51. Liu Y, Dilger JP. Opening rate of acetylcholine receptor channels. Biophys J. 1991; 60(2):424–32. PMID: 1717017

52. Li G, Sheng Z, Huang Z, Niu L. Kinetic mechanism of channel opening of the GluRDflip AMPA receptor. Biochemistry. 2005; 44(15):5835–41. PMID: 15823042

53. Li G, Pei W, Niu L. Channel-opening kinetics of GluR2Qflip AMPA receptor: A laser-pulse photolysis study. Biochemistry. 2003; 42(42):12358–66. PMID: 14567697

54. Hess B, Kutzner C, van der Spoel D, Lindahl E. GROMACS 4: algorithms for highly efficient, load-balanced, and scalable molecular simulation. J Chem Theory Comput. 2008; 4(3):435–47.

55. Jorgensen WL, Chandrasekhar J, Madura JD, Impey RW, Klein ML. Comparison of simple potential functions for simulating liquid water. J Chem Phys. 1983; 79(2):926–35.

56. Jorgensen WL, Maxwell DS, Tirado-Rives J. Development and testing of the OPLS all-atom force field on conformational energetics and properties of organic liquids. J Am Chem Soc. 1996; 118(45):11225–36.

57. Kaminski GA, Friesner RA, Tirado-Rives J, Jorgensen WL. Evaluation and reparametrization of the OPLS-AA force field for proteins via comparison with accurate quantum chemical calculations on peptides. J Phys Chem B. 2001; 105(28):6474–87.

58. Berger O, Edholm O, Jähnig F. Molecular dynamics simulations of a fluid bilayer of dipalmitoylphosphatidylcholine at full hydration, constant pressure, and constant temperature. Biophys J. 1997; 72 (5):2002–13. PMID: 9129804

59. Åqvist J. Ion-water interaction potentials derived from free energy perturbation simulations. J Phys Chem. 1990; 94(21):8021–4.

60. Pavlov M, Siegbahn PEM, Sandström M. Hydration of beryllium, magnesium, calcium, and zinc ions using density functional theory. J Phys Chem A. 1998; 102(1):219–28.

61. Loken C, Gruner D, Groer L, Peltier R, Bunn N, Craig M, et al. SciNet: lessons learned from building a power-efficient top-20 system and data centre. J Phys Conf Ser. 2010; 256(1):012026.